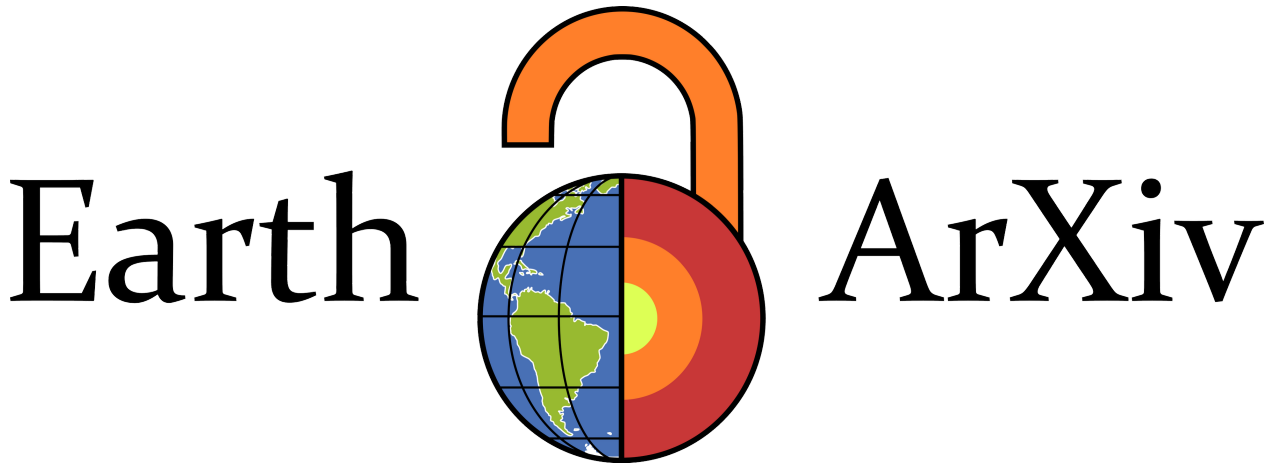

Detection of Point-Source Methane Enhancements from MethaneSAT Observations with Target-Driven Spectral Matching Algorithm

Yingqi Yan[1,2,3], Fei Li[1,2,3], Shiwei Sun[4], Shengxi Bai[1,2,3], Qidan Huang[1,2,3], Jiayi Liu[1,2,3] and Yongguang Zhang[1,2,3*]

[1]International Institute for Earth System Sciences, Jiangsu Center for Collaborative Innovation in Geographical Information Resource Development and Application, Nanjing University, Nanjing, Jiangsu 210023, China.

[2]Frontiers Science Center for Critical Earth Material Cycling, Nanjing University, Nanjing, Jiangsu 210023, China.

[3]Jiangsu International Joint Carbon Neutrality Laboratory, Nanjing, Jiangsu, 210023, China.

[4]Nanjing Innovation Institute for Atmospheric Sciences, Chinese Academy of Meteorological Sciences-Jiangsu Meteorological Service, Nanjing, Jiangsu 210041, China

[5]Jiangsu Key Laboratory of Severe Storm Disaster Risk / Key Laboratory of Transportation Meteorology of CMA, Nanjing, Jiangsu 210041, China

Corresponding author: Y. G. Zhang (ygz@nju.edu.cn)

Key Points:

- An updated matched filter method (BCMF) developed for sub-nanometer MethaneSAT methane retrievals.
- Nineteen methane point-source plumes detected and monitored across diverse facility types and emission scenarios.
- Our emission estimates show strong agreement with MethaneSAT flux products across identified sources.

Abstract

Methane is a potent greenhouse gas with large emissions often arising from localized point sources in industrial facilities. MethaneSAT, launched in 2024, observes the 1598-1683 nm band with sub-nanometer resolution and 100 m × 400 m footprints, enabling sensitive detection of methane absorption. We introduce an updated matched filter (BCMF) with covariance exclusion and a statistical correction for linearization

bias. Simulations and retrievals show that BCMF removes a ~20% underestimation, yielding unbiased enhancements. Across multiple emission scenarios, 19 plumes were detected and cross-section emission flux estimates agree with MethaneSAT proxy products (r=0.965, MAPE = 20.3%, n=16). These results demonstrate BCMF as a fast, robust approach for quantifying methane emissions with next-generation high-resolution satellite sensors.

Plain Language Summary

Methane is a powerful greenhouse gas that strongly contributes to near-term climate change. Many of the largest emissions arise from individual facilities such as oil and gas operations, landfills, and coal mines, making accurate detection and quantification essential for effective mitigation. MethaneSAT, launched in 2024, was designed to bridge the gap between regional greenhouse-gas monitors and fine-scale imaging spectrometers. It combines sub-nanometer spectral resolution with ground footprints of about 100 × 400 meters across a swath more than 200 kilometers wide. This configuration enables both regional mapping of methane and attribution of plumes to specific point sources. We developed an updated matched-filter method (BCMF) that reduces background noise and corrects a ~20% systematic underestimation, providing unbiased methane enhancements. Tests with simulations and MethaneSAT observations detected 19 point-source plumes, and fluxes from the cross-section flux (CSF) method showed strong agreement with MethaneSAT proxy products (r=0.965, MAPE = 20.3%, n=16). These results demonstrate BCMF as a fast and reliable tool for global monitoring of methane point sources with next-generation satellites.

1 Introduction

Methane is a potent greenhouse gas with a significant impact on climate change mitigation (IPCC, 2023). Anthropogenic methane emissions from the energy and waste sectors often originate from discrete point sources that can be identified and quantified (e.g., Cusworth et al., 2020; Cusworth et al., 2022; Reay et al., 2018). Hyperspectral remote sensing has emerged as a promising technique for detecting these point-source emissions, particularly with the recent advances in spectral and spatial resolution of spaceborne sensors (Jacob et al., 2022).

The matched filter (MF) is a widely used data-driven technique for detecting methane plumes, requiring minimal reliance on atmospheric or physical priors. Instead, it exploits a reference absorption kernel combined with background whitening to isolate plume signals (Thompson et al., 2015). The method has been demonstrated with airborne imaging spectrometers, such as AVIRIS (Duren et al., 2019), and more recently extended to spaceborne hyperspectral platforms, including PRISMA, EnMAP, EMIT and GF5, which provide spectral resolutions of 5-10 nm in the shortwave infrared methane absorption bands (Cusworth et al., 2019; Guanter et al., 2021; Li et al., 2024).

Emerging satellite missions, such as MethaneSAT, are designed to reduce the observational gap between coarse-resolution greenhouse gas sensors (e.g., TROPOMI) and general-purpose imaging spectrometers. MethaneSAT achieves this by integrating sub-nanometer spectral resolution with spatial sampling on the order of individual facilities, thereby enhancing sensitivity to column-integrated methane enhancements while preserving synoptic coverage (Miller et al., 2024). This design explicitly

addresses the trade-off between spatial resolution, spectral fidelity, and domain coverage, enabling detection of concentrated plumes that would be diluted at coarser scales while also retaining capability to constrain diffuse regional fluxes.

Here, we develop an optimized matched filter (BCMF) tailored to the fine spectral sampling (<1 nm) of advanced imaging spectrometers in the SWIR absorption bands. BCMF corrects systematic MF biases that arise at MethaneSAT spectral resolution and is applied to point-source methane plume retrievals. Applications to multiple facility-scale emission events demonstrate consistent detection performance and flux estimates within expected uncertainty bounds. These results confirm that the updated matched filter techniques remain robust under sub-nanometer spectral resolution, supporting their use for high-fidelity methane monitoring in forthcoming satellite missions.

2 Materials and Methods

2.1 MethaneSAT Instrument

MethaneSAT, launched on 4 March 2024 by the Environmental Defense Fund (EDF), operates in a sun-synchronous orbit at ~585 km altitude. It observes with a 21° field of view, yielding a nadir swath of ~210 km, and achieves a native ground sampling distance of ~100 m (across-track) by 400 m (along-track) at nadir (Fig. 1a). Each overpass provides a contiguous imaging domain of ~210 km × 210 km, allowing basin-scale mapping within a single scene. The payload consists of two passive infrared Littrow imaging spectrometers, each equipped with a 2k × 2k mercury–cadmium–telluride (HgCdTe, MCT) focal plane array, spanning 1249–1305 nm (O_2) and 1598–

1683 nm (CH_4/CO_2), respectively, with a signal-to-noise ratio (SNR) of ~190 under typical conditions (Rohrschneider, 2021).

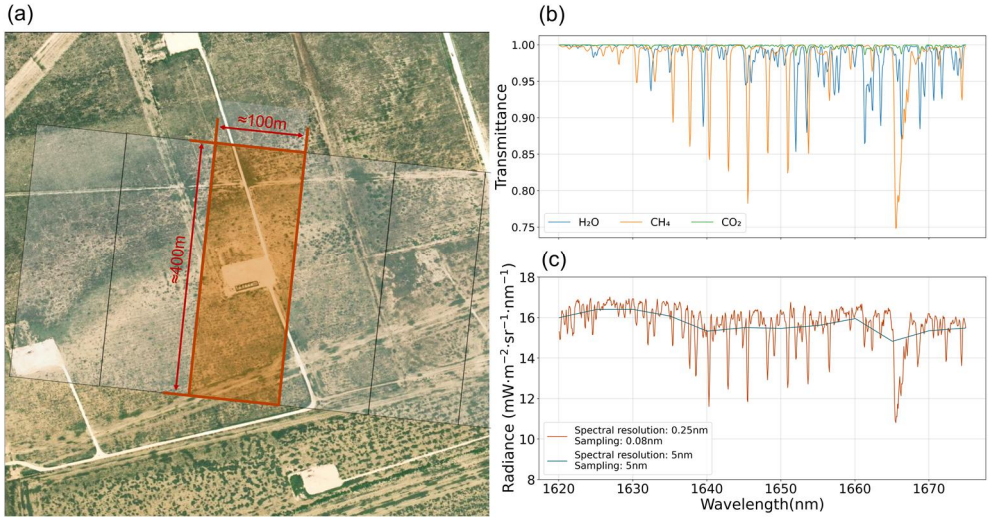

Figure 1. Spatial and spectral resolution characteristics of MethaneSAT. (a) Sub-regional spatial resolution enables precise tracking and attribution of methane emissions to specific point sources. (b) Methane absorption features within the retrieval window are shown by the transmittance spectrum. (c) Pixel-level radiance spectra, with the red line representing full-resolution radiance and the blue line showing the same radiance resampled to 5 nm resolution (comparable to airborne sensors such as AVIRIS or satellite sensors like EnMAP HSI). Higher spectral resolution allows clearer identification of absorption lines corresponding to the background atmospheric methane concentration, consistent with the features seen in the transmittance spectrum in (b).

For MethaneSAT, methane retrievals are performed in the 1592-1697 nm spectral band that is optimized for CH_4 quantification using the CO_2-proxy approach (see proxy implementation details in the Supporting Information Text S1). In the methane retrieval bands, MethaneSAT has a sampling interval of 0.08 nm and a spectral resolution of 0.25 nm. Compared with existing hyperspectral sensors, this resolution is substantially higher, allowing individual absorption lines within the window to be clearly resolved (Figs. 1b and 1c). Performance assessments with MethaneAIR, an airborne analogue with spectral capabilities similar to MethaneSAT, show that under the CO_2-proxy approach retrievals at 20 × 20 m^2 resolution achieve measurement precision typically

better than 2% and overall biases within ~1% (Miller et al., 2024). These capabilities enable quantification of concentrated point sources and diffuse emissions across major oil–gas basins, bridging the gap between coarse-resolution GHG imagers and facility-scale spectrometers. In addition to supporting the CO_2-proxy approach, MethaneSAT's advanced spectral configuration benefits matched filter retrievals, providing the foundation for the method presented in the following section. (Guanter et al., 2025).

2.2 **Bias Corrected Matched Filter (BCMF) Method**

The MF is a data-driven approach that detects methane column enhancements with low computational cost. Compared with full physics-based inversions, MF requires weaker priors—principally a reference absorption kernel and background whitening—rather than detailed local atmospheric constraints, which facilitates transfer across scenes and sensors (Foote et al., 2021; Thorpe et al., 2014).

MF treats the input scene as a Gaussian-distributed background field $L \sim \mathcal{H}(L_0, \Sigma)$, with methane absorption within the selected window modeled as a directional deviation from this distribution. By projecting each pixel onto the direction defined by the signal template t, the algorithm quantifies the degree to which the pixel deviates from the background along the absorption axis (Manolakis, 2004; Truslow and Manolakis, 2017). For a radiance input L, the column-enhancement estimate $\hat{a}$ is given as:

$$\hat{a} = \frac{(L - L_0)^T \Sigma^{-1} t}{t^T \Sigma^{-1} t} \quad (1)$$

where L_0 and Σ denote the mean and covariance of the radiance input L, and t is the unit absorption spectrum of methane. Details of parameters are provided in Text S2 of the Supporting Information.

Accurate and reliable estimation of the covariance Σ and target signature t is critical to MF performance (Theiler and Foy, 2006; Thompson et al., 2015). For MethaneSAT retrievals, we propose a bias-corrected MF (BCMF) method to correct systematic biases arising from the covariance Σ and target signature t.

In the method of MF, the covariance $\boldsymbol{\Sigma}$ characterizes the distribution of a blank background field without target signals. When the input data contain pixels with methane column enhancements, the covariance estimated from the radiance sequence becomes contaminated by the target signal. In the retrievals from hyperspectral spectral data, limited sample sizes and low pixel-to-channel ratios make the estimated background covariance particularly sensitive to the signal-induced contamination. We further discuss this specific mechanisms of contamination in Text S3 and Fig.S1 of the Supporting Information.

To mitigate this contamination, we adopt an exclusion approach, previously used in hyperspectral retrievals (Ayasse et al., 2019; Foote et al., 2020). To our knowledge, this is for the first time applied at hyperspectral resolution. Given that pixels containing column enhancements are sparse in the background, even when the input swath is aligned with the plume direction, their number generally does not exceed 20 pixels (corresponding to ~2 km of plume extent), which is less than 5% of the total. Accordingly, we remove the top 5% of pixels ranked by match filter response from the

158 covariance estimate to reduce potential signal contamination. This preserves most
159 background samples while improving the robustness of the covariance and enhancing
160 plume retrieval and detection; the effect of the covariance correction is shown in Figure
161 S2 and S3 of the Supporting Information.

162 The linearization of methane transmittance represents another source of systematic
163 error in the matched filter (Pei et al., 2023; Schaum, 2021). As a linear detector, the
164 original matched filter assumes the target signal t is proportional to the estimated
165 column enhancement $\hat{a}$,

166 $$L - L_0 = t \cdot \hat{a} \tag{2}$$

167 where t is defined as the derivative of methane transmittance T with respect to the
168 column enhancement a, scaled by the mean radiance L_0 (see Text S3 of the
169 Supporting Information):

170 $$t = L_0 \cdot \left.\frac{\partial T}{\partial a}\right|_{a=0} \tag{3}$$

171 Whereas, based on the Beer–Lambert law for the dependence of transmittance on
172 column enhancement, the relation between T and a is

173 $$T = \exp(k \cdot a), \quad \left.\frac{\partial T}{\partial a}\right|_{a=0} = k \tag{4}$$

174 with k denoting a coefficient representing the sampled absorption cross section.
175 From the definition of transmittance,

176 $$L - L_0 = (T - 1)L_0 \tag{5}$$

and combining Eq. (2) and Eq. (5) yields the analytical relation between the estimated $\hat{a}$ and the true column enhancement a

$$a = \frac{\log(k \cdot \hat{a} + 1)}{k} \tag{6}$$

Linearization of the matched filter at $a = 0$ causes the estimated column enhancement $\hat{a}$ to be systematically lower than the true value a, as expressed in Eq. (6). The fine spectral resolution of MethaneSAT enhances sensitivity to narrow absorption features, which makes this approximation particularly prone to bias. Figure S6 of the Supporting Information specifically illustrates this bias, which becomes pronounced when column enhancements exceed ~200 ppb and leads to increasing underestimation at higher concentrations. To balance computational efficiency with accuracy, we apply a statistical post-correction that mitigates this bias in high-emission cases. Because matched filtering operates in the whitened radiance domain, the values of k within a window are not directly accessible. To address this, we estimate k empirically through simulation. Prescribed column enhancements are injected into blank scenes, while covariance is computed from the pre-injection radiances to avoid signal contamination. Under these conditions, the retrieval bias relative to the injected truth arises solely from linearization, allowing *k* to be inferred from the truth–retrieval relationship. The fitting procedure is shown in Figure S5 of the Supporting Information, and the window-specific resulting k is then applied through Eq. (6) to correct the linearization-induced bias.

2.3 Estimation of methane emission flux

We estimated emission fluxes for detected plumes using the cross-section flux (CSF) method, which integrates concentration enhancement with the wind's normal component along transects approximately perpendicular to the flow (Varon et al., 2018; 2020). The method provides instantaneous emission estimates under the assumptions of a quasi-steady plume, nearly uniform winds across the transect, and negligible chemical loss and deposition.

As a first-order choice, we use ERA5 100 m winds to represent advection at typical plume-transport heights (~50–200 m). This level reduces the sensitivity to surface roughness and near-surface stability, and is broadly representative for elevated sources and buoyant rise when the effective plume height overlaps this layer. GEOS-FP and ERA5 10 m winds are also used as ancillary indicators for plume identification and screening. Methods for CSF-based emission estimation and the associated uncertainty diagnostics are provided in Supporting Information Text S4 and Figure S4.

3 Results and discussion

3.1 Validation with WRF-LES Simulations

Retrieval performance depends strongly on the choice of spectral window. Because the number of spatial samples in a MethaneSAT push-broom scan is fixed (~560 pixels), expanding the retrieval window increases the signal-to-noise ratio but destabilizes background covariance estimates when the number of spectral channels approaches the spatial dimension (Ayasse et al., 2023). To balance this trade-off, we selected two windows (1636–1652 nm and 1664–1670 nm) with a width of 6 nm.

Within 1636–1652 nm, only CH_4 absorption sub-bands were retained to maximize sensitivity while minimizing noise (Fig. 2a). Comparative retrieval results are provided in Figure S7.

To further evaluate flux retrieval, we used plume simulations generated with the WRF large-eddy simulation (WRF-LES) model (Fig. 2b). WRF-LES explicitly resolves boundary-layer turbulence and scalar transport at meter-scale resolution, producing realistic plumes that capture dispersion and dilution processes (Matheou, 2016; Jongaramrungruang et al., 2019). A series of plumes with prescribed emission rates of 1000 kg h^{-1} were simulated, and corresponding hyperspectral scenes were generated with a forward radiative transfer model (see details in model setup in Supporting Information, Test S6). To represent diverse observing conditions, three background scenes were selected from oil and gas basins in North America, spanning variations in surface properties, atmospheric state, and acquisition time (Fig. 2c).

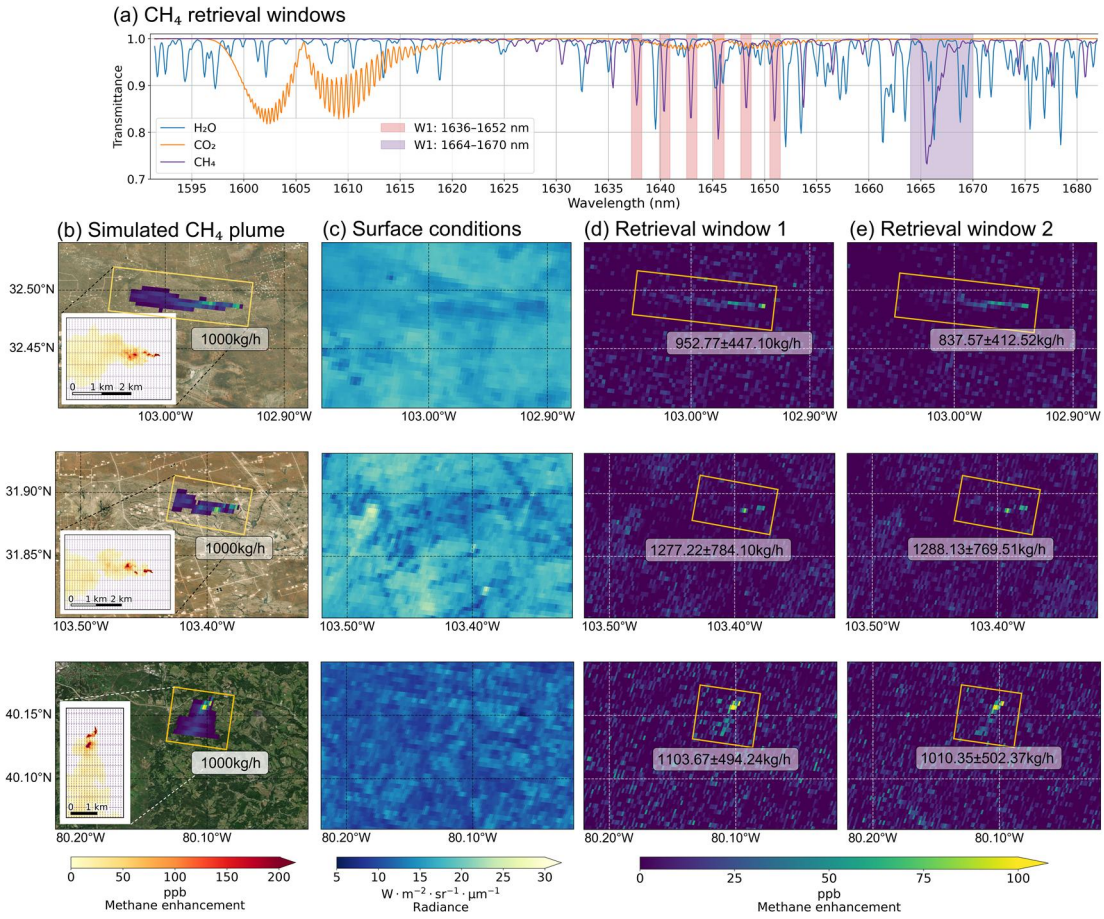

Figure 2. Algorithm sensitivity derived from WRF-LES simulation tests. (a) Two spectral windows used for methane retrieval, highlighted in red (Window 1) and purple (Window 2); (b) a WRF-LES plume scenario at 10 m resolution (emission rate 1000 kg h^{-1}; wind speed 3 m s^{-1}), down-sampled to MethaneSAT scale and superimposed on background radiance using the corresponding line-of-sight transmittance to produce an observation-equivalent field; the inset shows the pre-sampling plume footprint; Basemap: Esri World Imagery(Esri & Maxar, 2021); (c) surface albedo proxy at 1622 nm radiance; (d–e) MF-retrieved column-mean enhancements ΔXCH_4 in the two windows and the CSF-based emission estimate Q, broadly consistent in spatial morphology and magnitude ranking with the sampled column enhancements in (b). The first two backgrounds are in the Permian Basin and the third in the Marcellus Shale—both major oil-and-gas provinces in North America. The insertion locations are illustrative for surface/scene representativeness and algorithm sensitivity only, and do not imply the presence of actual point sources or emissions of similar magnitude.

We applied the BCMF to these WRF-LES–based forward simulations and estimated emission fluxes using the CSF method. Retrieval accuracy was evaluated using two criteria: (1) the agreement between retrieved pixel-scale column enhancements and simulated plume structures, and (2) the consistency between inferred

and reference emission fluxes. For Window 1, retrieved column enhancements yielded nRMSE = 32.4%, nMBE = 20.1%, and a Pearson correlation of 0.862 relative to the reference plume. For Window 2, corresponding values were nRMSE = 28.8%, nMBE = 18.2%, and a Pearson correlation of 0.878. In both cases, retrieved emission fluxes deviated from the prescribed 1000 kg h^{-1} release by less than 30% (Fig. 2d, e). These results demonstrate that the BCMF can robustly retrieve methane point-source emissions at the spatial scale of MethaneSAT, with reliable detection for plumes exceeding ~1 t h^{-1} - a threshold jointly constrained by the instrument's spectral resolution and spatial sampling.

The BCMF performance was further assessed through synthetic injection simulations to test robustness across a broader range of emission scenarios (see Supporting Information, Text S4). Across both retrieval windows, the standard deviation (1σ) of retrievals over blank scenes remained below 30 ppb, and intrinsic algorithmic noise was constrained within 40 ppb (1σ). Given that natural background methane columns typically fluctuate by ~30–40 ppb (1σ), the algorithmic noise is comparable to atmospheric background uncertainty. For 100 ppb enhancements, retrieval standard deviation was ~20 ppb, and for 200 ppb enhancements it remained within 40 ppb (1σ). These results indicate that the BCMF maintains sensitivity to plume structures and associated emission sources, providing unbiased column enhancement estimates. Localized signals exceeding the background variability by more than one standard deviation can be robustly distinguished from background noise, confirming the method's capability for reliable plume detection and quantification.

Overall, these results demonstrate that the optimized BCMF retrieval applied to MethaneSAT observations can robustly detect and quantify facility-scale methane emissions under realistic atmospheric and surface conditions. By balancing retrieval window design with instrument constraints and validating performance against high-resolution plume simulations, this framework establishes a pathway for accurate flux estimation in forthcoming satellite missions.

3.2 Detection and identification of point-sources methane plumes

Using the BCMF method, we detected methane emissions from multiple oil and gas facilities in North America and a waste management facility. MethaneSAT's high spatial resolution preserves plume morphology, enabling reliable source attribution (Fig. 3). Plumes were extracted using a structured workflow that suppressed noise, removed small artifacts, and selected wind-aligned enhancements (see Supporting Information Text S7).

Over the Marcellus shale basin on 5 September 2024, 13 methane sources were identified that is preliminarily attributed to well pad activity. Under weak winds (2-3 m s^{-1}), plumes extended 2-5 km and showed peak enhancements of 44-213 % above background, with dispersion patterns consistent with the identified sources. Plume morphology was strongly modulated by wind and topography. On flat terrain with stronger winds (~5 m s^{-1}), large-flux events (>1 t h^{-1}) produced plumes >10 km downwind, though enhancements were distributed across multiple pixels, limiting low-flux detection. In complex terrain or under weak winds, advection weakened and vorticity-driven dispersion dominated, with terrain-induced shear and recirculation

folding and meandering plumes. Nonetheless, localized methane accumulation produced strong column enhancements, enabling detection despite greater uncertainty in source attribution. For example, event #15 over Natural Buttes, Utah (17 January 2025) showed ~500 ppb enhancements within 2 km from a valley source under low wind, producing a non-typical plume morphology at the given spatial resolution.

The 1.60–1.70 µm window reduced interference from surface absorptions (e.g., carbonates) relative to the 2.3 µm band. However, water, moist surfaces, artificial materials, topography-induced BRDF, shading, and thin clouds or haze can introduce smoother, quasi-uniform continuum biases. To further evaluate algorithm performance under diverse scenarios, retrievals were conducted over a Persian Gulf waste management facility on 5 September 2024 and a Permian Basin scene on 11 September 2024, representing flat terrain with stronger winds (Fig. 3). These retrievals confirmed four plumes (#14 and #16–#18), demonstrating robust detection across varying environmental conditions.

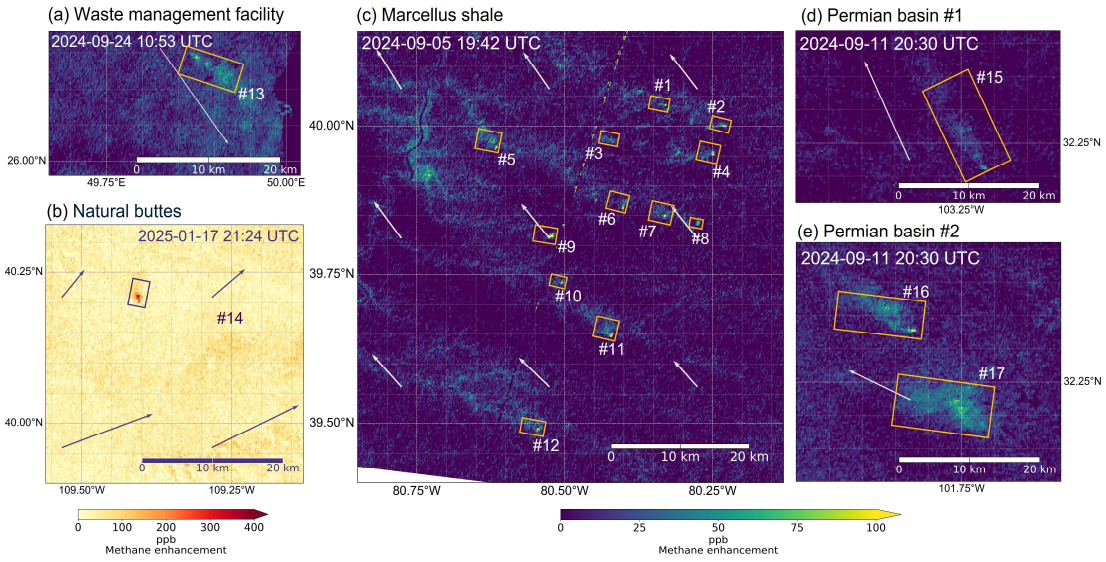

Figure 3. BCMF retrieval scenes and plume detection. (a) A coastal waste-management site along the Persian Gulf; (b) a gas well in Utah, USA, showing localized build-up of column-mean CH_4 under weak winds and terrain influence. At the current 100 m × 400 m sampling scale, peak $\Delta XCH_4 \approx 500$ ppb (relative to background). (c–e) Multiple methane plumes detected over representative oil–gas settings in the Marcellus Shale and the Permian Basin. Rectangles mark automatically detected plumes; arrow lengths indicate the 1 h downwind advection distance derived from ERA5 100 m winds, with direction and magnitude reflecting near-surface flow.

3.3 Cross-Validation with MethaneSAT official CO_2 Proxy Method

Snapshot emission rates for the 16 detected plumes were estimated using the CSF method combined with ERA5 100 m winds, with uncertainties quantified via first-order linear error propagation (Fig. 4 and Text S4 of Supporting Information). At the current spatial sampling, pixel footprints are large, introducing potential source-attribution challenges: in dense regions, a single plume may encompass multiple emitters, and multiple facilities may fall within one pixel. Nevertheless, in the emission scenes analyzed here, plume morphology remains clearly identifiable, and when combined with local wind fields, typically constrains the responsible source to the 100 m scale.

Of the 16 identified point sources, 14 coincide with MethaneSAT-reported sources (Fig. 4). Fluxes derived from matched-filter retrievals with CSF range 1-15 t h^{-1}, consistent with large emissions from energy and waste facilities observed by spaceborne sensors. Source-by-source comparison with the CO_2-proxy approach (Chulakadabba et al., 2023) demonstrates high agreement (Pearson r = 0.965, MAPE = 20.3%, RMSE = 1.23 t h^{-1}) with a York fit slope of ~0.88, indicating a modest low bias attributable to residual linearization effects, mitigated by post-correction (Fig. 4). Cross-validation against MethaneSAT point-source fluxes also shows agreement within uncertainties, with no significant systematic offset.

Differences relative to MethaneSAT-reported fluxes are expected given the use of different wind products and forward BCMF estimates of column enhancement. Notably, our forward column-enhancement estimates generally match the MethaneSAT CO_2-proxy product, suggesting remaining discrepancies arise primarily from the flux-estimation step (e.g., wind fields and CSF setup) rather than retrieval accuracy (Fig.4). Overall, our findings confirm that our optimized matched-filter scheme is well suited for MethaneSAT-scale retrievals. Flux uncertainties are dominated by wind representativeness and transect–wind alignment, particularly at 100 m × 400 m spatial sampling scale.

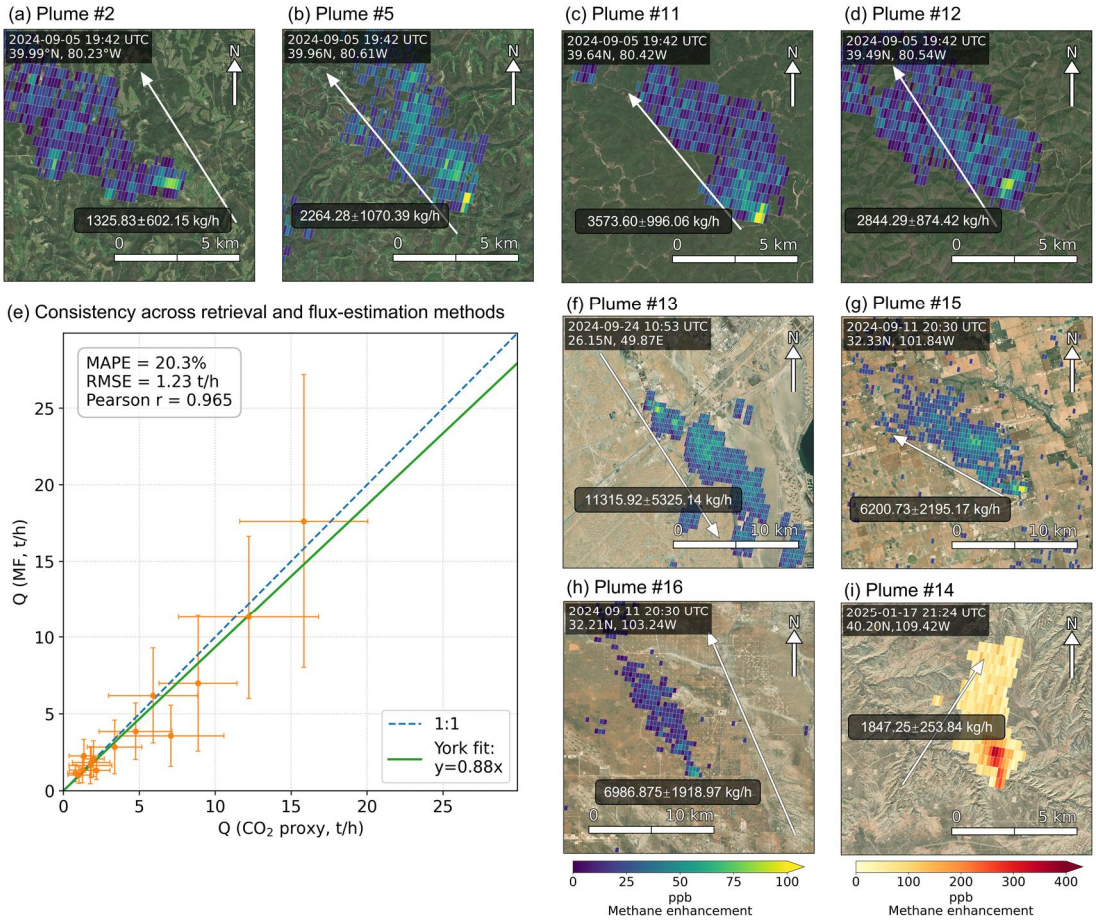

Figure 4. CSF-based plume emission estimates and validation. (a–d, f–i) Representative plume snapshots extracted from MF retrievals using morphological filtering and thresholding, corresponding to the plumes in Figure 3. Arrows indicate the 1 h downwind advection distance

derived from ERA5 100 m winds (direction and length reflect near-surface flow). Basemap: Esri World Imagery(Esri & Maxar, 2021) (e) Cross-validation against the MethaneSAT point-source emission product: source-by-source comparison between MF plus CSF estimates and the official product shows overall agreement with no obvious systematic bias. Details on these plumes are provided in the Supporting Information Table 1.

4 Conclusions

Our results demonstrate that the matched filter algorithm, originally developed for general hyperspectral sensors, can be successfully applied to sub-nanometer-scale methane column enhancement retrievals. Systematic errors in BCMF application to MethaneSAT observations were mitigated through covariance contamination correction and subsequent linearization adjustments, reducing bias from background variability and model–measurement mismatches and improving plume retrieval robustness. The BCMF-retrieved enhancements show strong consistency with total column results derived from the CO_2-proxy method. Leveraging MethaneSAT data, we optimized the matched filter for high-resolution scenes using covariance and linearization corrections. Validation across 16 point sources in four scenes spanning diverse surface types, meteorological conditions, and facility categories demonstrates reliable detection and flux estimation. Emission rates derived via the CSF method agree closely with MethaneSAT-reported fluxes, confirming robustness across environmental and source variability. These findings establish that our BCMF approach is well suited for sub-nanometer spectral data and can accurately retrieve methane point-source emissions at facility scales and as suitable for MethaneSAT's ultraspectral resolution.

Data Availability

ERA5 reanalysis data are available from the Copernicus Climate Data Store at https://cds.climate.copernicus.eu/. GEOS-FP data are available from NASA's Global Modeling and Assimilation Office at https://gmao.gsfc.nasa.gov/GMAO_products/. MethaneSAT L1B, L2, and L4 products are available via Google Earth Engine and Google Cloud Storage under the Public Preview framework at https://www.methanesat.org/.

Acknowledgments

This research was supported by the National Science Foundation of China (U24A20590), the National Key Research and Development Program of China (2024YFB3910201), and the Fundamental Research Funds for the Central Universities - Cemac "GeoX" Interdisciplinary Program (No. 2024300245). We thank the MethaneSAT team, led by the Environmental Defense Fund and partner institutions, for providing the L1B, L2, and L4 data products through Google Earth Engine and Google Cloud Storage. MethaneSAT, the first NGO-led methane-monitoring satellite, was designed to reveal invisible emissions from fossil fuel operations and strengthen accountability in climate action. Although contact was lost in June 2025, the data collected during its mission (2023–2024) remain openly accessible under the Public Preview framework and continue to provide a valuable resource for methane research and mitigation efforts.

References

Intergovernmental Panel on Climate Change (IPCC) (2023), *Climate Change 2023: Synthesis Report. Summary for Policymakers*, IPCC, Geneva, Switzerland, 34 pp., doi: https://doi.org/10.59327/IPCC/AR6-9789291691647.001.

Ayasse, A. K., D. Cusworth, K. O'Neill, J. Fisk, A. K. Thorpe, and R. Duren (2023), Performance and sensitivity of column-wise and pixel-wise methane retrievals for imaging spectrometers, *Atmos Meas Tech*, *16*(24), 6065–6074, doi: https://doi.org/10.5194/amt-16-6065-2023.

Ayasse, A. K., P. E. Dennison, M. Foote, A. K. Thorpe, S. Joshi, R. O. Green, R. M. Duren, D. R. Thompson, and D. A. Roberts (2019), Methane Mapping with Future Satellite Imaging Spectrometers, *Remote Sens-Basel*, *11*(24), doi: https://doi.org/10.3390/rs11243054.

Chulakadabba, A., et al. (2023), Methane point source quantification using MethaneAIR: a new airborne imaging spectrometer, *Atmos Meas Tech*, *16*(23), 5771–5785, doi: https://doi.org/10.5194/amt-16-5771-2023.

Cusworth, D. H., R. M. Duren, A. K. Thorpe, E. Tseng, D. Thompson, A. Guha, S. Newman, K. T. Foster, and C. E. Miller (2020), Using remote sensing to detect, validate, and quantify methane emissions from California solid waste operations, *Environ Res Lett*, *15*(5), doi: https://doi.org/10.1088/1748-9326/ab7b99.

Cusworth, D. H., et al. (2019), Potential of next-generation imaging spectrometers to detect and quantify methane point sources from space, *Atmos Meas Tech*, *12*(10), 5655–5668, doi: https://doi.org/10.5194/amt-12-5655-2019.

Cusworth, D. H., et al. (2022), Strong methane point sources contribute a disproportionate fraction of total emissions across multiple basins in the United States, *P Natl Acad Sci USA*, *119*(38), doi: https://doi.org/10.1073/pnas.2202338119.

Duren, R. M., et al. (2019), California's methane super-emitters, *Nature*, *575*(7781), 180–+, doi: https://doi.org/10.1038/s41586-019-1720-3.

Esri, & Maxar. (2021). Esri world imagery [Dataset]. ArcGIS REST Services Director y. Retrieved from https://services.arcgisonline.com/ArcGIS/rest/services/World_Image ry/MapServer

Foote, M. D., P. E. Dennison, A. K. Thorpe, D. R. Thompson, S. Jongaramrungruang, C. Frankenberg, and S. C. Joshi (2020), Fast and Accurate Retrieval of Methane Concentration From Imaging Spectrometer Data Using Sparsity Prior, *Ieee T Geosci Remote*, *58*(9), 6480–6492, doi: https://doi.org/10.1109/Tgrs.2020.2976888.

Foote, M. D., P. E. Dennison, P. R. Sullivan, K. B. O'Neill, A. K. Thorpe, D. R. Thompson, D. H. Cusworth, R. Duren, and S. C. Joshi (2021), Impact of scene-specific enhancement spectra on matched filter greenhouse gas retrievals from imaging spectroscopy, *Remote Sens Environ*, *264*, doi: https://doi.org/10.1016/j.rse.2021.112574.

Guanter, L., I. Irakulis-Loitxate, J. Gorroño, E. Sánchez-García, D. H. Cusworth, D. J. Varon, S. Cogliati, and R. Colombo (2021), Mapping methane point emissions with the PRISMA spaceborne imaging spectrometer, *Remote Sens Environ*, *265*, doi: https://doi.org/10.1016/j.rse.2021.112671.

Guanter, L., J. Warren, M. Omara, A. Chulakadabba, J. Roger, M. Sargent, J. E. Franklin, S. C. Wofsy, and R. Gautam (2025), Detection and quantification of methane plumes with the MethaneAIR airborne spectrometer, *Atmos Meas Tech*, *18*(15), 3857–3872, doi:

https://doi.org/10.5194/amt-18-3857-2025.
Jacob, D. J., et al. (2022), Quantifying methane emissions from the global scale down to point sources using satellite observations of atmospheric methane, *Atmos Chem Phys*, *22*(14), 9617–9646, doi: https://doi.org/10.5194/acp-22-9617-2022.
Jongaramrungruang, S., C. Frankenberg, G. Matheou, A. K. Thorpe, D. R. Thompson, L. Kuai, and R. M. Duren (2019), Towards accurate methane point-source quantification from high-resolution 2-D plume imagery, *Atmos Meas Tech*, *12*(12), 6667–6681, doi: https://10.5194/amt-12-6667-2019.
Li, F., S. X. Bai, K. R. Lin, C. X. Feng, S. W. Sun, S. H. Zhao, Z. T. Wang, W. Zhou, C. Y. Zhou, and Y. G. Zhang (2024), Satellite-Based Surveys Reveal Substantial Methane Point-Source Emissions in Major Oil & Gas Basins of North America During 2022-2023, *J Geophys Res-Atmos*, *129*(19), doi: https://10.1029/2024JD040870.
Manolakis, D. (2004), Detection algorithms for hyperspectral imaging applications: A signal processing perspective, *2003 Ieee Workshop on Advances in Techniques for Analysis of Remotely Sensed Data*, 378–384.
Matheou, G., and K. W. Bowman (2016), A recycling method for the large-eddy simulation of plumes in the atmospheric boundary layer, *Environ Fluid Mech*, *16*(1), 69–85, doi: https://10.1007/s10652-015-9413-4.
Miller, C. C., et al. (2024), Methane retrieval from MethaneAIR using the CO2 proxy approach: a demonstration for the upcoming MethaneSAT mission, *Atmos Meas Tech*, *17*(18), 5429–5454, doi: https://doi.org/10.5194/amt-17-5429-2024.
Pei, Z. P., G. Han, H. Q. Mao, C. H. Chen, T. Q. Shi, K. Y. Yang, X. Ma, and W. Gong (2023), Improving quantification of methane point source emissions from imaging spectroscopy, *Remote Sens Environ*, *295*, doi: https://doi.org/10.1016/j.rse.2023.113652.
Reay, D. S., P. Smith, T. R. Christensen, R. H. James, and H. Clark (2018), Methane and Global Environmental Change, *Annu Rev Env Resour*, *43*, 165–192, doi: https://doi.org/10.1146/annurev-environ-102017-030154.
Rohrschneider, R. R. W., S.; Franklin, J. E.; Benmergui, J.; Soto, J.; Davis, S. B. (2021), The MethaneSAT mission, in *35th Annual Small Satellite Conference (SSC21-II-05)*, edited, pp. 1–7, Logan, Utah, USA.
Schaum, A. (2021), A uniformly most powerful detector of gas plumes against a cluttered background, *Remote Sens Environ*, *260*, doi: https://doi.org/10.1016/j.rse.2021.112443.
Theiler, J., and B. R. Foy (2006), Effect of signal contamination in matched-filter detection of the signal on a cluttered background, *Ieee Geosci Remote S*, *3*(1), 98–102, doi: https://doi.org/10.1109/Lgrs.2005.857619.
Thompson, D. R., et al. (2015), Real-time remote detection and measurement for airborne imaging spectroscopy: a case study with methane, *Atmos Meas Tech*, *8*(10), 4383–4397, doi: https://doi.org/10.5194/amt-8-4383-2015.
Thorpe, A. K., C. Frankenberg, and D. A. Roberts (2014), Retrieval techniques for airborne imaging of methane concentrations using high spatial and moderate spectral resolution: application to AVIRIS, *Atmos Meas Tech*, *7*(2), 491–506, doi: https://doi.org/10.5194/amt-7-491-2014.
Truslow, E., and D. Manolakis (2017), Plume Detection with Emphasis on Phenomenology,

Signal Models, and Exploitation Algorithms, *Int Geosci Remote Se*, 1332–1335.

Varon, D. J., D. J. Jacob, D. Jervis, and J. McKeever (2020), Quantifying Time-Averaged Methane Emissions from Individual Coal Mine Vents with GHGSat-D Satellite Observations, *Environ Sci Technol*, *54*(16), 10246–10253, doi: https://doi.org/10.1021/acs.est.0c01213.

Varon, D. J., D. J. Jacob, J. McKeever, D. Jervis, B. O. A. Durak, Y. Xia, and Y. Huang (2018), Quantifying methane point sources from fine-scale satellite observations of atmospheric methane plumes, *Atmos Meas Tech*, *11*(10), 5673–5686, doi: https://doi.org/10.5194/amt-11-5673-2018.

Supporting Information for

Detection of Point-Source Methane Enhancements in MethaneSAT Observations via Target-Driven Spectral Matching

Y. Q. Yan[1,2,3], F. Li[1,2,3], S. W. Sun[4], S. X. Bai[1,2,3], Q. D. Huang[1,2,3], J. Y. Liu[1,2,3] and Y. G. Zhang[1,2,3*]

[1]International Institute for Earth System Sciences, Jiangsu Center for Collaborative Innovation in Geographical Information Resource Development and Application, Nanjing University, Nanjing, Jiangsu 210023, China.

[2]Frontiers Science Center for Critical Earth Material Cycling, Nanjing University, Nanjing, Jiangsu 210023, China.

[3]Jiangsu International Joint Carbon Neutrality Laboratory, Nanjing, Jiangsu, 210023, China.

[4]Key Laboratory of Transportation Meteorology of China Meteorological Administration, Nanjing Joint Institute for Atmospheric Sciences, Nanjing, China.

Contents of this file

Text S1.

CO_2 proxy method

The CO_2 proxy method estimates the total column density of methane by leveraging CO_2 absorption in the P and R branches near 1595–1618 nm and CH_4 $2\nu_3$ absorption features within 1629–1654 nm. This approach is based on several key assumptions: that methane and carbon dioxide share the same optical path length; that the background concentration of CO_2 is uniform and stable, allowing it to serve as a reference gas; and that common atmospheric and surface influences—such as aerosols, clouds, viewing geometry, and surface reflectance—affect CH_4 and CO_2 in a spectrally correlated manner, enabling their effects to be largely canceled or corrected through ratio-based retrievals.

The SPLAT method, developed by the Harvard–Smithsonian Center for Astrophysics, is first used to retrieve the vertical column densities of CH_4 and CO_2, denoted as N_{CH_4} and N_{CO_2} respectively. Specifically, SPLAT optimizes the state vector x by minimizing the following cost function,

$$J(x) = \left(y - F(x)\right)^{\mathrm{T}} S_o^{-1}\left(y - F(x)\right) + \gamma^{-2}(x - x_a)^{\mathrm{T}} S_a^{-1}(x - x_a)$$

The cost function $J(x)$ minimizes a trade-off between the residuals of the forward model fit $F(x)$ to observations y and the deviation of the state vector x from a priori estimates x_a. The observation covariance matrix S_o and the a priori covariance matrix S_a respectively quantify the uncertainties in observations and in the a prior knowledge. A regularization factor γ further balances the relative contributions of the two terms in the cost function.

The state vector includes scaling factors for the CH_4 and CO_2 dry-air mole fraction profiles(x_{CH_4}, x_{CO_2}),a water vapor column scaling factor (x_{H_2O}), surface pressure (x_{ps}), a temperature offset from the a priori profile (x_T), and two sets of polynomial coefficients used to scale the spectral albedo within each retrieval window ($x_{alb,\,CO_2}, x_{alb,\,CH_4}$), based on Lambertian-equivalent reflectance near 1622.5 nm. Among these, x_{CH_4} and x_{CO_2} are further used to compute the vertical column density N_{CH_4} and N_{CO_2}.

The proxy-derived XCH_4 is then obtained by scaling the ratio N_{CH_4}/N_{CO_2} with an a priori estimate of the dry-air column-averaged CO_2 mole fraction $XC0_{2,0}$.

$$XCH_4 = \frac{N_{CH_4}}{N_{CO_2}} XC0_{2,0}$$

The key advantage of the proxy approach lies in its ability to improve CH_4 retrieval accuracy by reducing sensitivity to surface albedo and aerosol scattering errors, which similarly affect both gas retrievals but cancel in the ratio.

Text S2.

Additional Details on MF Calculation

The MF approach exploits the characteristic methane absorption features in the SWIR spectral region to retrieve column enhancements. Under the simplified radiative transfer framework, the observed radiance L can be approximated as:

$$L = L_0 \cdot \tau(\sigma, \alpha, l) \quad (1)$$

where L_0 is the hypothetical background radiance under typical atmospheric methane levels, and τ is the transmittance determined by the methane column enhancement α. In the SWIR region, where aerosol and scattering effects are relatively weak, this approximation enables a linearized treatment of the radiance difference as a function of methane enhancement:

$$L - L_0 \approx t \cdot a \quad (2)$$

Here, the template absorption signal t is obtained as

$$t = L_0 \cdot \frac{\sigma_\tau}{\sigma_a}|_{a=a_{\mathrm{ref}}} \quad (3)$$

The unit absorption spectrum $\frac{\sigma_\tau}{\sigma_a}|_{a=a_{\mathrm{ref}}}$ was generated using high-resolution line-by-line absorption coefficients from the HITRAN database, and convolved with the instrument spectral response function to match sensor characteristics. To account for aerosol impacts within the retrieval window, a wavelength-dependent scaling was applied based on radiative transfer simulations 6S model.

Previous methane absorption spectra used for general-purpose hyperspectral sensors were typically simulated using the MODTRAN model; however, the spectral

precision achieved by MODTRAN cannot meet the spectral sampling interval requirements of MethaneSAT. Here, we consider utilizing high-resolution absorption cross-sections derived from the HITRAN database, which are then spectrally resampled to MethaneSAT's spectral resolution to compute the methane unit absorption strength required for the matched filter algorithm.

According to the Beer–Lambert law governing methane gas absorption, the transmittance can be expressed as:

$$\tau = exp(\sigma \cdot n_{air} \cdot \alpha \cdot amf \cdot H) \tag{3}$$

where σ denotes the methane absorption cross-section at the corresponding spectral band obtained from the HITRAN database under a reference temperature of 296 K and standard atmospheric pressure; n_{air} is the atmospheric molecular number density; α represents the stable column enhancement of methane concentration at the bottom of the troposphere with height H (typically 8000 m); amf (Air Mass Factor) is a correction accounting for the influence of the radiative transfer path factor which is given by

$$amf = \frac{1}{\cos(SZA)} + \frac{1}{\cos(VZA)} \tag{5}$$

SZA and VZA represent the solar zenith angle and the view zenith angle, respectively, and are determined by the observation geometry during satellite imaging.

The partial derivative with respect to the column enhancement a is given by

$$\frac{\sigma_\tau}{\sigma_a} = \sigma \cdot n_{air} \cdot amf \cdot H \cdot exp(\sigma \cdot n_{air} \cdot \alpha \cdot amf \cdot H) \tag{6}$$

Due to the dilution effect of MethaneSAT's relatively larger pixel size on the column enhancement, the methane column enhancements in the scene are generally weak. Therefore, we consider $a_{\text{ref}} = 0$ as the linearization point for the Beer–Lambert law expansion. At this point, we have:

$$\frac{\sigma_\tau}{\sigma_a}|_{a=0} = \sigma \cdot n_{air} \cdot amf \cdot H \tag{7}$$

The process of resampling methane transmittance to the sensor's spectral resolution can be discretized and regarded as a weighted averaging of transmittance within each spectral band. For the discretized and normalized spectral response function $R(\lambda_j)$, The transmittance resampled to MethaneSAT's spectral resolution is given by:

$$\tilde{\tau}(\lambda_i) = \sum_j \tau(\lambda_j) \cdot R(\lambda_j) \tag{8}$$

Since linear operations do not affect differentiation, the partial derivative of the transmittance can be expressed as:

$$\frac{\sigma_{\tilde{\tau}}}{\sigma_a}|_{a=0} = \sum_j \frac{\sigma_\tau}{\sigma_a}|_{a=0} \cdot R(\lambda_j) = \sum_j \sigma(\lambda_j) \cdot n_{air} \cdot amf \cdot H \cdot R(\lambda_j) \tag{9}$$

The sampled derivative $\frac{\sigma_{\tilde{\tau}}}{\sigma_a}|_{a=0}$ is then used as the unit target absorption to calculate the methane target absorption spectrum.

Text S3.

Signal-induced contamination of the covariance

Matched filtering assumes that pixels used for covariance estimation reflect signal-free background statistics. When those pixels contain non-negligible target or correlated absorbers, they contaminate the background covariance and degrade filter performance. The contamination can be decomposed into two components:

$$\Sigma = \Sigma_0 + a^2 \cdot tt^T + a \cdot t\zeta^T + a \cdot \zeta t^T$$

The term $a^2 \cdot tt^T$ is a rank-1 inflation along the target direction, whereas ($a \cdot t\zeta^T + a \cdot \zeta t^T$) is a cross-coupling term arising from weak correlation between the target and background interferers. In a MF model, pure inflation cancels to first order, whereas cross-coupling rotates the whitened template away from the target subspace, thereby weakening the filter's response to column-enhancement signals.

For MethaneSAT, where pixel sampling is relatively coarse and the number of input pixels per scene is limited (≈560 pixels per scan line), covariance contamination in the matched filter becomes more pronounced and can bias column-enhancement amplitudes low. We mitigate this using a two-pass exclusion scheme: assuming plume sparsity at the current resolution (≤5% of pixels traceable to a plume), we perform an initial retrieval, mask the top 5% of MF responses, and recompute the background covariance from the remaining pixels before the final pass. This forward elimination reduces signal-induced contamination of the background covariance and the associated low bias.

Text S4.

Emission Flux Estimation

The cross-sectional flux (CSF) integrates methane column enhancements across a transect perpendicular to the plume axis, combined with the cross-section normal wind to estimate snapshot emissions. It is applicable when the plume resides within the mixed layer, chemical loss is negligible over the transport time, the source is quasi-steady, and the transect spans the full plume.

Let y be the arc-length along the transect, $u_n(y)$the wind component normal to the transect, $\Delta XCH_4(y)$ the methane dry-air column-mean enhancement (mol/mol; multiply ppb by 1e-9), $P_S(y)$ the surface pressure (Pa), g the gravitational acceleration (m/s^2), and $\frac{M_{CH_4}}{M_{air}} \approx 0.554$. The snapshot emission rate Q (kg/s) is:

$$Q = \int u_n(y)\Delta XCH_4(y)\frac{P_S(y)}{g}\frac{M_{CH_4}}{M_{air}}dy \quad (10)$$

Discrete pixel form (pixel width Δy_i):

$$Q = \sum_{i=1}^{N} u_{n,i}\ \Delta X_{CH4,i}\ \frac{P_{s,i}}{g}\frac{M_{CH4}}{M_{air}}\ \Delta y_i \quad (11)$$

We quantify flux uncertainty using first-order linear error propagation. The dominant contributors are: (i) errors in the cross-sectional column-enhancement retrieval $\Delta X_{CH4,i}$, including background removal, and (ii) uncertainty in the transect-normal wind $u_{n,i}$, encompassing wind-speed and directional projection errors. Unless stated otherwise, these error terms are treated as approximately independent.

We assume that column-enhancement retrieval errors are independent across pixels and, consequently, approximately independent across downwind transects. For each transect $k = 1, \dots, K$, we compute Q_k and use the dispersion of $\{Q_k\}$ to quantify the forward retrieval algorithmic uncertainty σ_{alg}.

For the transect-normal wind $u_{n,i}$, guided by typical error ranges reported for ERA5 and GEOS-FP in plume-transport flux applications, we adopt a representative mid-value of 40% as a relative uncertainty. Treating wind as a multiplicative, near common-mode error along a transect,

$$\sigma_{\text{wind}} = f_u \, |\bar{Q}|, \qquad f_u = 0.40 \tag{12}$$

Assuming independence between these components, the total uncertainty is combined in quadrature:

$$\sigma_{\text{total}} = \sqrt{\left(\sigma_{\text{alg}}^2 + \sigma_{\text{wind}}^2\right)} \tag{13}$$

Text S5.

WRF-LES Simulation and methane point-source quantification

We employed the Large-Eddy Simulation (LES) capability of the Weather Research and Forecasting (WRF) model to explicitly resolve turbulent motions in the atmospheric boundary layer and the transport of passive scalars. In LES mode, WRF directly resolves the dominant, energy-containing eddies, while smaller subgrid-scale turbulence is parameterized through a turbulence kinetic energy (TKE) closure. The model domain typically extends over the lower troposphere with horizontal grid spacing of tens of meters, enabling the simulation of plume dispersion, dilution, and near-surface mixing processes that cannot be captured in coarser mesoscale configurations. Boundary conditions and surface fluxes are prescribed from larger-scale meteorological analyses, allowing WRF-LES to represent realistic wind, stability, and surface-layer dynamics for scenario-based plume experiments. This framework provides a controlled, physically consistent environment to study methane point-source dispersion and evaluate retrieval algorithms.

We configured WRF in LES mode to generate synthetic methane plume fields for algorithm evaluation. The simulations were conducted at 10 m × 10 m spatial resolution over the lower boundary layer and subsequently aggregated to the effective ground sampling distance of MethaneSAT (100 m × 400 m). A constant emission rate of 1000 kg h^{-1} was prescribed from a point source under a wind speed of 3 m s^{-1}, producing plumes representative of controlled release conditions. LES methane fields were then vertically integrated to pressure-weighted column enhancements (ΔXCH_4) relative to an upwind background, defined as

$$\Delta X_{\mathrm{CH_4}} = \frac{1}{P_s}\sum_{i=1}^{N}\left(\frac{\Delta m_{\mathrm{CH_4},i}}{M_{\mathrm{CH_4}}}\frac{g}{\Delta p_i}M_{\mathrm{air}}\Delta p_i\right) \quad (14)$$

where $\Delta m_{\mathrm{CH_4},i}$ is the methane column mass increment in layer i (kg m^{-2}), $M_{\mathrm{CH_4}}$ = 0.01604 kg mol^{-1} is the molar mass of methane, M_{air} = 0.028965 kg mol^{-1} is the molar mass of dry air, Δp_i is the pressure thickness of layer i (Pa), P_s is the surface pressure (Pa), and g=9.81 m s^{-2} is gravitational acceleration.

A forward radiative transfer model then used these ΔXCH₄ fields to compute band transmittance and top-of-atmosphersssse radiances in the chosen retrieval windows, and the resulting absorption signatures were superimposed on the radiance spectra of three background scenes from distinct North American oil and gas basins. These synthetic scenarios, while not reflecting actual emission events or levels at specific facilities, provide a controlled framework to test the performance of the matched filter at MethaneSAT's spatial scale.

Text S6.

Simplified Radiative Transfer Model and Synthetic injection simulation

We adopt a simplified radiative transfer model tailored to MethaneSAT's SWIR window. Surface reflectance is treated as a Lambertian term with wavelength-dependent albedo, while atmospheric absorption is represented by multiplicative transmittances for gases and thin cloud/haze. The top-of-atmosphere radiance $L_{\mathrm{TOA}}(\lambda)$ is approximated a

$$L_{\mathrm{TOA}}(\lambda) \approx E_0(\lambda)\,T_{\downarrow}(\lambda)\,\rho(\lambda)\,\frac{\mu_0}{\pi}\,T_{\uparrow}(\lambda) + L_{\mathrm{path}}(\lambda) \quad (15)$$

Where $E_0(\lambda)$ is the extraterrestrial spectral irradiance, $T_{\downarrow}(\lambda)$ is the downward atmospheric transmittance (gases and thin cloud/haze), $\rho(\lambda)$ is the effective surface reflectance (Lambertian, wavelength dependent), μ_0 is the cosine of the solar zenith angle, $T_{\uparrow}(\lambda)$ is the upward atmospheric transmittance (gases and thin cloud/haze), and $L_{\mathrm{path}}(\lambda)$ is the path radiance due to scattering along the line of sight.

For the blank-background radiance , and neglecting $L_{\mathrm{path}}(\lambda)$—which is acceptable in the SWIR under low-aerosol conditions—the column enhancement along the transmission path can be treated as acting on $L_{\mathrm{TOA}}(\lambda)$through the transmittance factors given by the Beer–Lambert law (as in Eq. (3)).

Synthetic injection simulation is a key method used throughout this study (also see Figure S2, S5) to evaluate algorithm performance and correction effectiveness. Because the matched filter targets methane transmittance signals deviating from the background, the approach begins with blank background scenes, typically selected from MethaneSAT pixels without visible plumes. For a prescribed set of column enhancements, transmittance spectra are calculated using the Beer–Lambert law (as in Eq. (3)) and sequentially injected into each pixel of the background scenes. For each injection, the matched filter retrieval is performed on the modified pixel, yielding the retrieved enhancement corresponding to the injected signal. This design allows controlled evaluation of the algorithm's detection and retrieval performance under diverse

conditions while minimizing confounding factors.

Text S7.

Plume identification and masking

Plume identification is performed on the matched-filter score field S and yields a binary mask used in downstream analyses. We first apply total-variation (TV) denoising to suppress high-frequency, near-zero-mean noise while preserving coherent gradients, and then standardize locally so that each pixel value is expressed as a robust z-score relative to its neighborhood.

Candidate regions are extracted by adaptive thresholding with a baseline of one standard deviation $\sigma_{\mathcal{N}(i)}$ above the local mean $\mu_{\mathcal{N}(i)}$;

$$S_i \geq \mu_{\mathcal{N}(i)} + 1\,\sigma_{\mathcal{N}(i)} \tag{16}$$

To remove residual speckles while maintaining plume edges, we apply a morphological opening (erosion followed by dilation) with a 3×3 structuring element and optionally discard very small connected components. Each surviving candidate is then screened for physical plausibility based on (i) alignment of its major axis with the prevailing wind, (ii) the presence of plume-like downwind gradients, and (iii) proximity to a plausible source facility. Candidates that satisfy these criteria form the final plume mask, and we export this mask together with component metadata (centroid, orientation, length, width, mean/peak score) for source attribution and CSF transect construction.

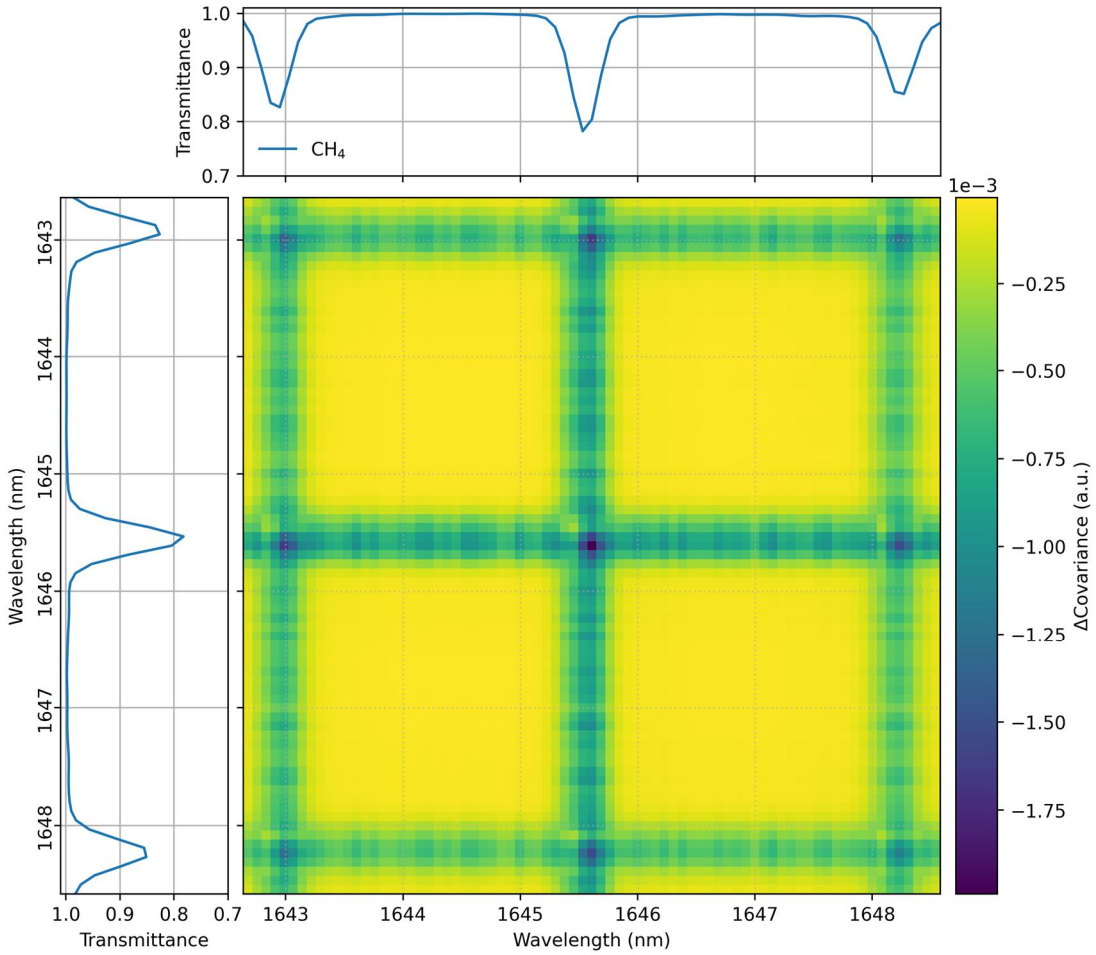

Figure S1. Covariance contamination by injected signal. Example for a 1642–1649 nm window (560 pixels along-track): we compare background covariance estimated from a blank scene with that after injecting a 100 ppb column enhancement into a single, randomly chosen pixel. Although the perturbation to the covariance is small in magnitude, matrix inversion amplifies its effect and degrades the matched-filter response (via cross-coupling in the whitened space).

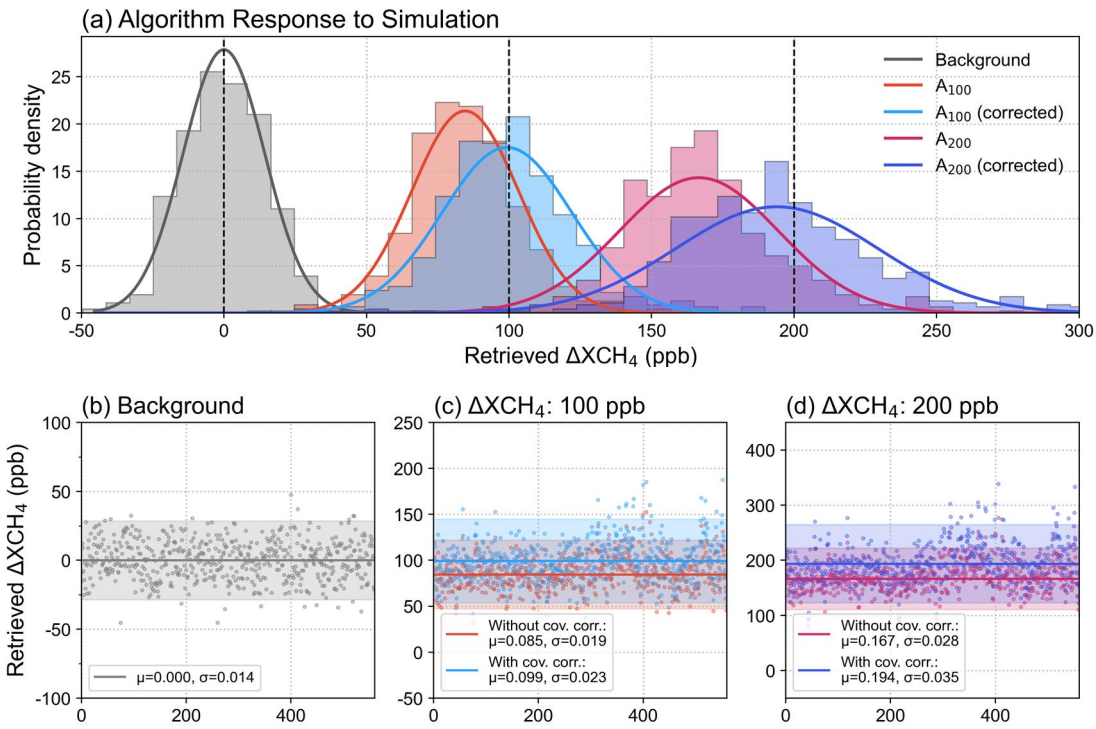

Figure S2. Impact of covariance contamination on matched-filter (MF) retrievals and its correction. A random pixel was selected in a blank background; synthetic column enhancements were imposed and the covariance was re-estimated to assess MF bias and the efficacy of correction. (a) Distributions of retrieved results before and after correction across different enhancement levels (e.g., A_{100}, A_{200}): red denotes contaminated (pre-correction), blue denotes iterative post-correction. (b) MF response in the blank-background case (e.g., mean and spread) for comparison. (c) Scatter results for A_{100} with its corrected values, A_{100} (corrected); (d) scatter results for A_{200} with A_{200} (corrected). Covariance correction markedly reduces the contamination-driven low bias; a slight underestimation remains at larger enhancements (e.g., 200 ppb) due to linearization.

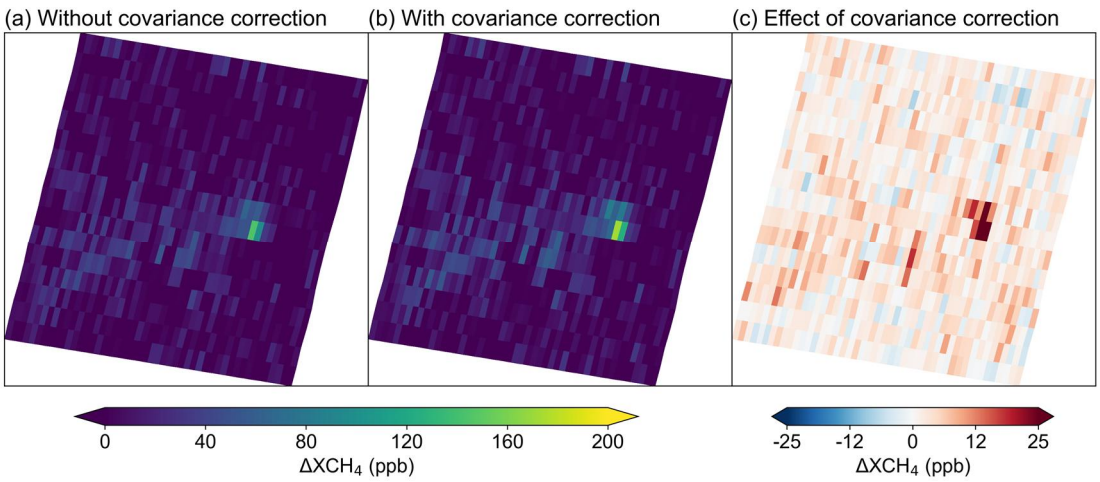

Figure S3. Impact of covariance contamination on matched filter (MF) retrievals and its correction. (a) ΔXCH_4 before covariance correction. (b) ΔXCH_4 after correction. (c) Change (after − before). Without correction, column enhancements are biased low by approximately 10–30% for this case.

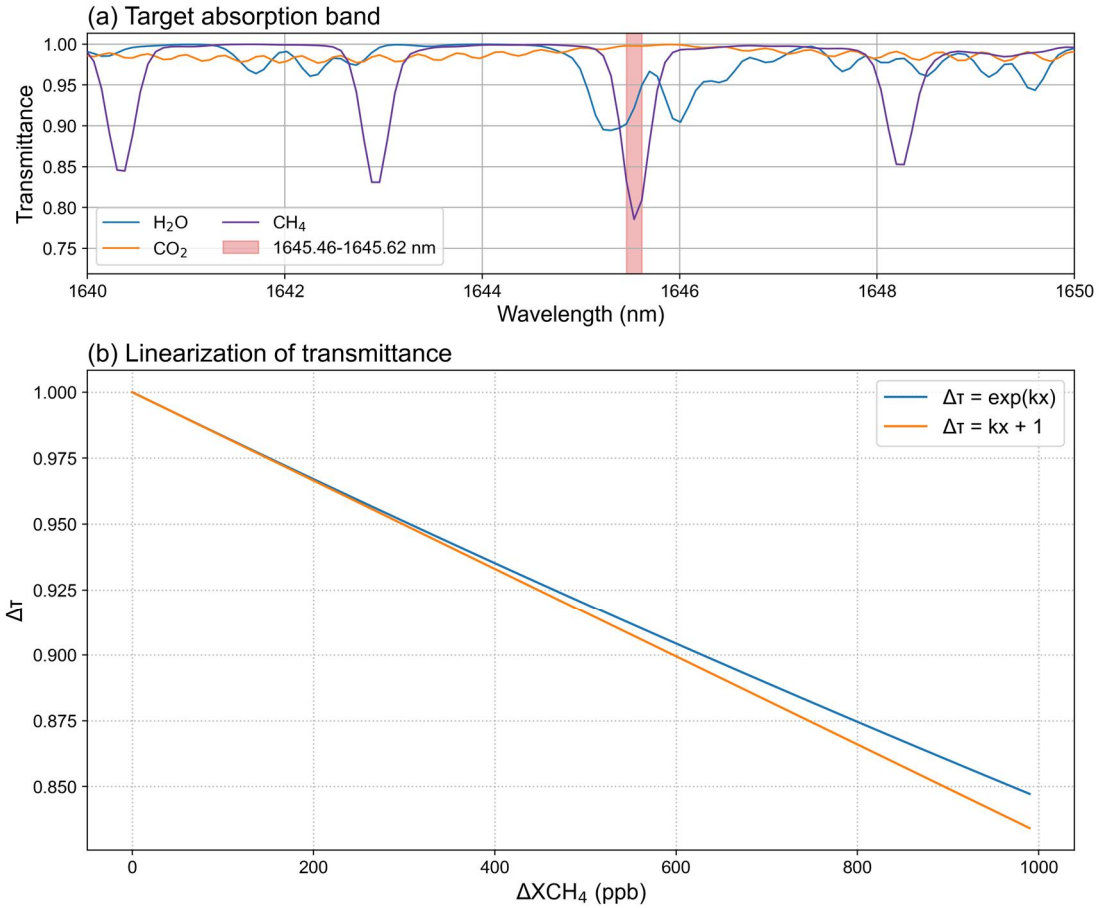

Figure S4. Deviation between MF linearization and the true transmittance–column enhancement relationship. The deviation grows with increasing column enhancement and biases high-end ΔXCH_4 estimates. (a) A major CH_4 absorption trough in the MethaneSAT window (near 1645.5 nm). (b) Comparison of the MF linear approximation (yellow) and the transmittance–column enhancement curve from the Beer–Lambert law (blue). At larger ΔXCH_4, the linear model overestimates the transmittance change, leading to an underestimation of the column enhancement. See SI for methods and parameters.

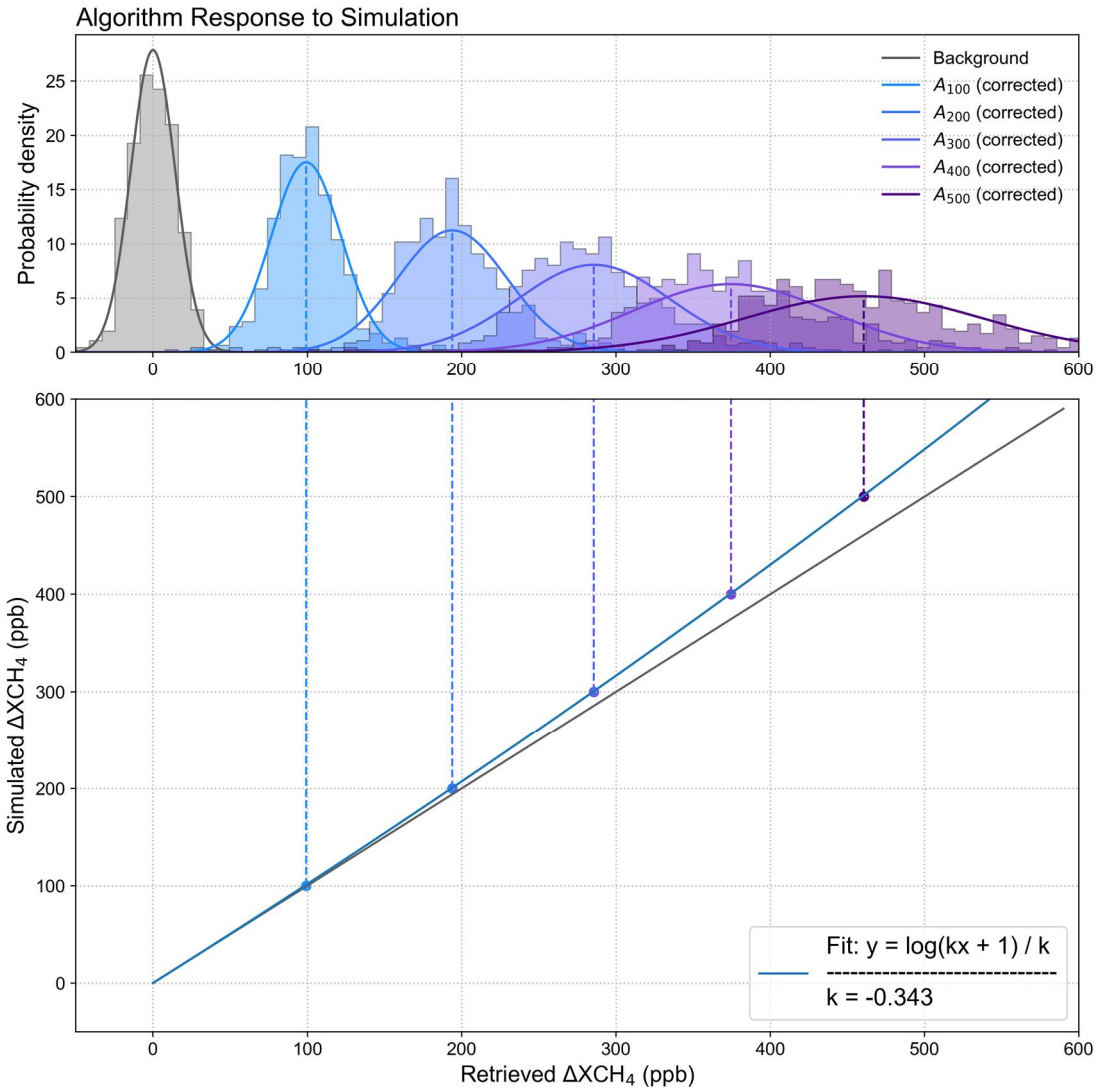

Figure S5. Simulation-based back-correction of linearization bias. Synthetic column enhancements of 100–600 ppb were randomly imposed on blank-background pixels to assess systematic bias in MF-retrieved ΔXCH_4. For each level, retrievals were approximately Gaussian; we used the distribution mean as the response. We then fitted response-imposed enhancement using the mismatch between the Beer–Lambert transmittance–enhancement curve and the MF linear approximation, yielding a back-correction curve. The fit performs well over 100–600 ppb and is applied to reduce underestimation at high ΔXCH_4; see SI for details.

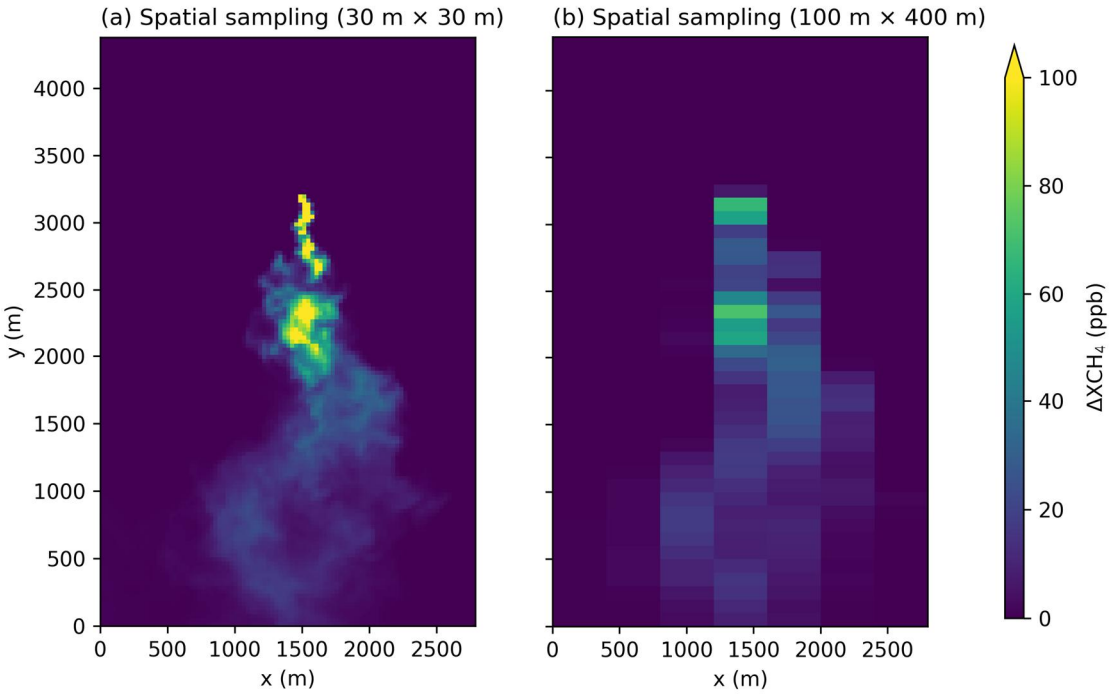

776

777 **Figure S6. Sampling of simulated plumes.** We used WRF-LES, configured with local
778 surface roughness, to simulate a set of methane plumes. The native resolution is 10 m x
779 10 m, and the fields were down-sampled to the sensor scale.

780

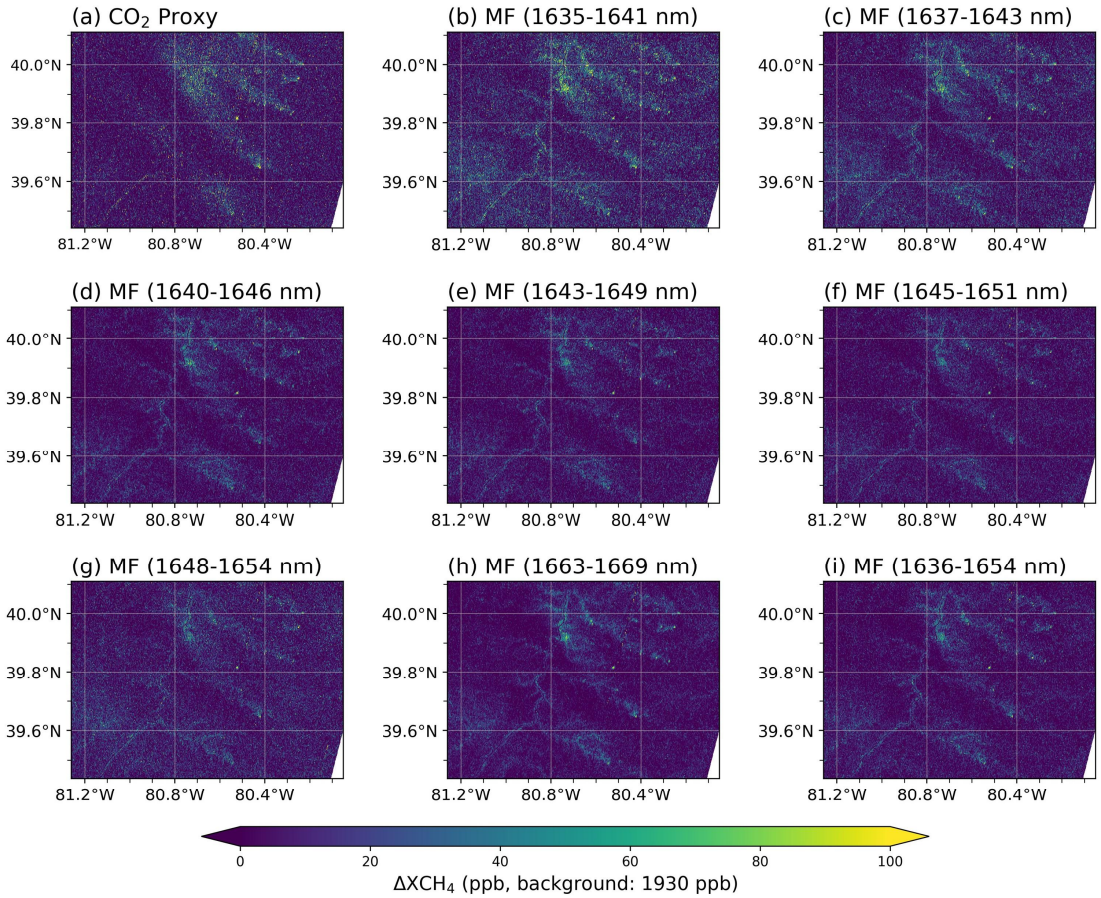

Figure S7. MF retrievals across spectral bands vs the CO_2 proxy. (a) CO_2-proxy column enhancement ΔXCH_4 relative to background XCH_4 = 1930 ppb (XCH_4 taken as the upwind mean). (b–h) MF retrievals using 6 nm sub-windows centered on major CH_4 lines. (i) MF result within 1636-1654 nm after masking the six dominant absorption lines. Overall, bands h and i maintain high SNR while remaining consistent with the CO_2-proxy reference.

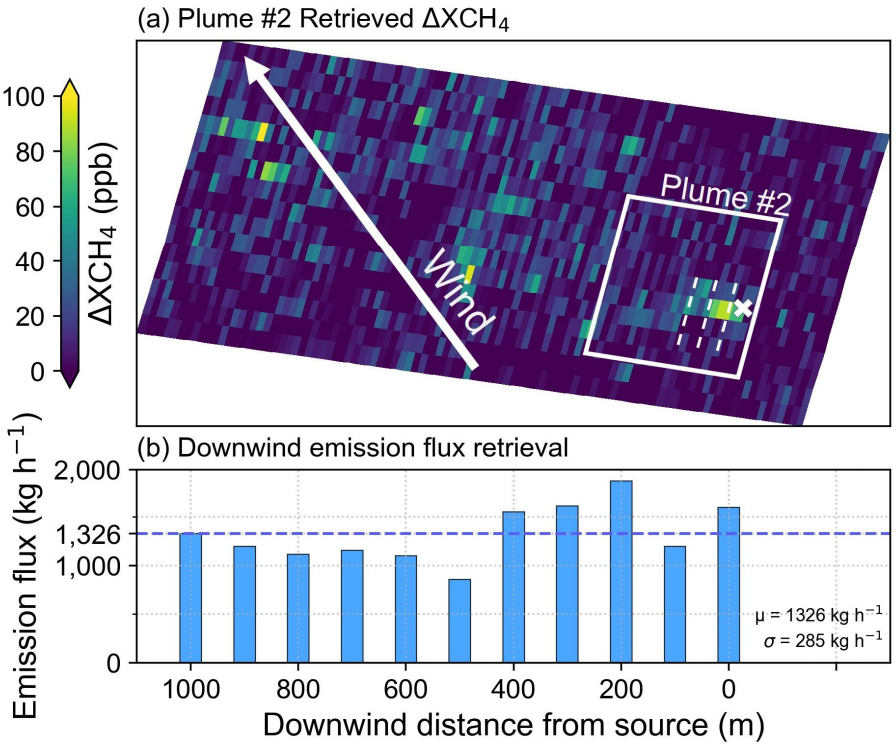

788

789 **Figure S8. Emission-rate estimation.** (a) Arrows show the 1 h downwind advection
790 distance from ERA5 100 m winds; the detected target plume is outlined by a rectangle;
791 transects are indicated by dashed lines; the point source is marked with "x". (b) Using the
792 CSF method, emission rates Q are computed from ten transects placed 1000 m downwind
793 and perpendicular to the plume axis; the mean across transects is taken as the point-
794 source estimate. Note that the plume axis may deviate from the wind direction due to
795 wind-field uncertainty and downsampling effects.

796

797

Table S1 Estimated methane emission fluxes from point sources, where Q (CO2 proxy) denotes the emission flux derived by MethaneSAT using the CO_2 proxy combined with the DI method, and Q (MF) represents the flux estimated using the MF and CSF methods.

Id	Datetime	Loc	Q (CO_2 proxy)	Q (MF)	Wind Speed
1	2024-09-05 19:42 UTC	40.03N, 80.32W	1014.26±720.80 kg/h	1021.89±546.82 kg/h	2.14 m/s
2	2024-09-05 19:42 UTC	39.99N, 80.23W	2173.70±896.65 kg/h	1325.83±602.15 kg/h	2.14 m/s
3	2024-09-05 19:42 UTC	39.97N, 80.42W	1257.11±866.14 kg/h	1343.16±816.76 kg/h	2.12 m/s
4	2024-09-05 19:42 UTC	39.95N, 80.25W	1779.20±1411.14 kg/h	1654.62±1196.48 kg/h	1.98 m/s
5	2024-09-05 19:42 UTC	39.96N, 80.61W	1335.20±968.96 kg/h	2264.28±1070.39 kg/h	2.12 m/s
6	2024-09-05 19:42 UTC	39.85N, 80.40W		1543.88±924.77 kg/h	2.12 m/s
7	2024-09-05 19:42 UTC	39.86N, 80.33W		2417.28±1052.80 kg/h	1.98 m/s
8	2024-09-05 19:42 UTC	39.84N, 80.27W	4758.41±2404.78 kg/h	3865.33±1844.72 kg/h	2.12 m/s
9	2024-09-05 19:42 UTC	39.81N, 80.52W	1968.47±722.70 kg/h	2080.88±1170.55 kg/h	2.12 m/s
10	2024-09-05 19:42 UTC	39.73N, 80.50W	788.68±501.98 kg/h	1144.57±556.04 kg/h	1.96 m/s
11	2024-09-05 19:42 UTC	39.64N, 80.42W	7062.17±3502.88 kg/h	3573.60±1992.12 kg/h	1.96 m/s
12	2024-09-05 19:42 UTC	39.49N, 80.54W	3367.00±1796.72 kg/h	2844.29±1748.84 kg/h	1.56 m/s
13	2024-09-24 10:53 UTC	26.15N, 49.87E	12196.77±4597.03 kg/h	11315.92±5325.14 kg/h	6.56 m/s
14	2025-01-17 21:24 UTC	40.20N,109.42W	1821.66±1239.08 kg/h	1847.25±1007.68 kg/h	1.64 m/s
15	2024-09-11 20:30 UTC	32.21N,103.24W	5896.65±2933.04 kg/h	6200.73±3095.17 kg/h	4.93 m/s
16	2024-09-11 20:30 UTC	32.33N,101.84W	8867.39±2573.30 kg/h	6986.875±4418.97 kg/h	2.78 m/s
17	2024-09-11 20:30 UTC	32.22N,101.70W	15832±4221 kg/h	17606.69±9585.302 kg/h	2.78 m/s